Nanoscale

Remote homoepitaxy of ZnO microrods across graphene layers

Journal:	*Nanoscale*
Manuscript ID	NR-ART-10-2018-008084.R1
Article Type:	Paper
Date Submitted by the Author:	12-Nov-2018
Complete List of Authors:	Jeong, Junseok; Sejong University Min, Kyung-Ah; Sejong University, Department of Physics and Graphene Research Institute Shin, Dong Hoon; Ewha Womans University, Department of Physics Yang, Woo-Seok; KETI, Yoo, J.; Los Alamos National Laboratory, Lee, Sang Wook; Ewha Womans University, Department of Physics Hong, Suklyun; Sejong University, Department of Physics Hong, Young Joon; Sejong University, Nanotechnology & Advanced Materials Engieering

SCHOLARONE™
Manuscripts

`

Remote homoepitaxy of ZnO microrods across graphene layers†

Junseok Jeong,‡[a,b,c] Kyung-Ah Min,‡[b,c,d] Dong Hoon Shin,[e] Woo Seok Yang,[f] Jinkyoung Yoo,[g] Sang Wook Lee,[e] Suklyun Hong*[b,c,d] and Young Joon Hong*[a,b]

[a] *Department of Nanotechnology & Advanced Materials Engineering, Sejong University, Seoul 05006, Republic of Korea*

E-mail: yjhong@sejong.ac.kr

[b] *Graphene Research Institute–Texas Photonics Center International Research Center (GRI–TPC IRC), Sejong University, Seoul 05006, Republic of Korea*

[c] *Graphene Research Institute, Sejong University, Seoul 05006, Republic of Korea*

[d] *Department of Physics and Astronomy, Sejong University, Seoul 05006, Republic of Korea*

E-mail: hong@sejong.ac.kr

[e] *Department of Physics, Ewha Womans University, Seoul 03760, Republic of Korea*

[f] *Nano Materials Research Center, Korea Electronics Technology Institute, Seongnam, Gyeonggi-do 13509, Republic of Korea*

[g] *Center for integrated Nanotechnologies, Los Alamos National Laboratory, Los Alamos, NM 87545, United States*

†Electronic supplementary information (ESI) available: Supplementary figures with the details of Raman spectroscopic analysis for graphene layers, cross-sectional transmission electron microscopy images, DFT-calculated atomic structure and charge density difference, scanning electron microscopy images for substrate regeneration.

‡These authors contributed equally to this work

`

GRAPHICAL ABSTRACT: Vertical and horizontal ZnO microrods are grown on *c*-and *c*-plane ZnO across graphene interlayer, owing to charge transfer through graphene, and the remote homoepitaxial microrods were exfoliated for substrate regeneration.

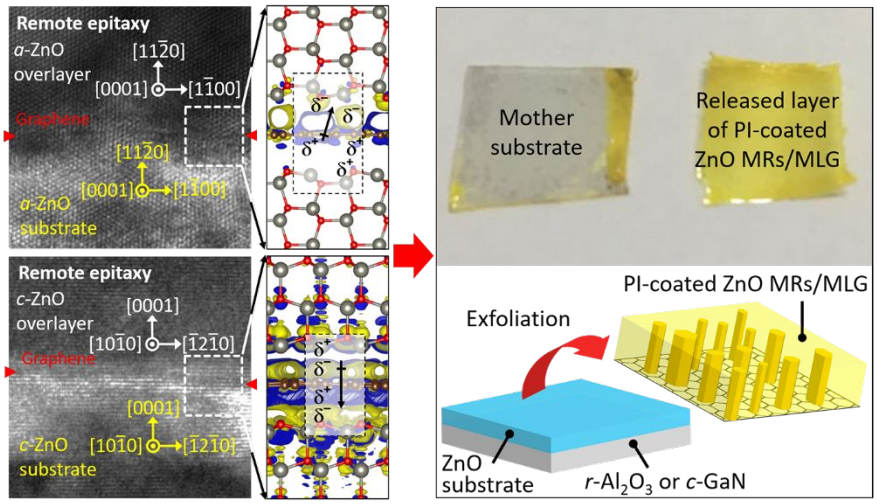

ABSTRACT: Two-dimensional atomic layered materials (2d-ALMs) have been emerging candidates for the use as epitaxial seed substrates toward transferrable epilayers. However, the micrometer-sized domain of 2d-ALMs precludes the practical use in the epitaxy because of causing crystallographical in-plane disordering of overlayer. Ultrathin graphene can penetrate the electric dipole momentum from underlying crystal layer to graphene surface so that drives to crystallize overlayer at an initial growth stage for substantial energy saving. This study demonstrates the remote homoepitaxy of ZnO microrods (MRs) on ZnO substrates across graphene layers via hydrothermal method. Despite of the presence of poly-domain graphene in between ZnO substrate and ZnO MRs, the MRs were epitaxially grown on *a*- and *c*-plane ZnO substrates, whose in-plane alignments were homogeneous within a wafer size. The transmission electron microscopy revealed a homoepitaxial relationship between the overlayer MRs and the substrate. The density-functional theory calculations suggested that the charge redistribution occurring near graphene induces the electric dipole formation, so the

`

attracted adatoms lead to formation of the remote homoepitaxial overlayer. Due to a strong potential field caused by long-range charge transfer given from the substrate, even the use of bi-layer and tri-layer graphene resulted in the remote homoepitaxial ZnO MRs. The effect of substrate crystal planes is also theoretically and empirically investigated. The ability of the graphene, which can be released from the mother substrate without covalent bonds, was utilized to transfer the overlayer MR arrays. This method opens a way of producing well aligned, transferrable epitaxial nano/microstructure arrays while regenerating the substrate for cost-saving device manufacturing.

KEYWORDS: Epitaxy, graphene, ZnO, hydrothermal growth, density functional theory calculations

`

■ Introduction

Epitaxy, which is a way that crystal growth yields single-crystalline semiconductor films or crystallographically aligned nanostructures on substrates, has been enabled to produce high-performance electronic and optoelectronic devices (e.g., field effect transistors, laser or light-emitting diodes, *etc*.) with high carrier mobility and quantum efficiency.[1-5] Since the conventional epitaxy is achieved by forming strong covalent bonds at the interface between the overlayer and the substrate, the technique limits a choice of substrate materials in terms of a small lattice misfit and single crystallinity to obtain high-quality overlayers with reduced density of an extended crystal defect generating from the interface.[6] After epitaxial growth, the substrate plays important roles in mechanically supporting the overlayer for handling in the post-growth fabrication process, and being the insulation and/or conduction platform for the epitaxial devices to operate the overlayer electronics and optoelectronics. On the contrary, for purposes of economical device production, high-performance device manufacturing, and flexible device fabrication, it is often desirable that the epitaxial overlayers are detached from the substrates via sacrificial layer etching and laser lift-off techniques.[7-9] However, these procedures inevitably involve damage to the overlayer devices, due to the highly corrosive and high photon power-assisted congruent melting conditions required to peel them off from strong covalent bonds.[10,11]

Recently, two-dimensional atomic layered materials (2d-ALMs, *i.e*., graphene, and hexagonal boron nitride) have been utilized as substrates for semiconductor epitaxy,[1,12-24] and graphene has been highly exploited because of its excellent physical properties, including good electrical and thermal conductivity, high optical transparency, amphoteric *n*- or *p*-type doping, and high elastic modulus.[25-29] As for the deposition of semiconductor on graphene, the honeycomb lattice of graphene rules the interfacial lattice configuration and symmetry of overlayer for heteroepitaxial relation. For example, CdTe,[30] CdS thin films,[31] ZnO buffer

`

nanowalls (or nanorods),[1,32] ZnO monolayer,[33] and vertical InAs nanowires[21,34] showed 30°-rotated in-plane hexagonal epitaxial relation with respect to the seed graphene layer even without interfacial covalent bonds, whose growth is refereed as the van der Waals (vdW) epitaxy. Vertical GaN nanowires on graphene showed that six sidewall facets were parallel to the zigzag edges of graphene, which were strained to accommodate a –3.1% in-plane misfit ensuring a certain lattice coincidence for substantial interfacial stress release, and remarkedly the nanowire number density decreased with increasing the graphene thickness due to the elastic energy stored in the interface that can elevates the nucleation activation energy barrier.[35] For gold catalyst-assisted Ge nanowire growth, the graphene substrate provided a platform enabling control of growth direction along either in-plane or out-of-plane orientation by changing the growth temperature and hydrochloric gas flow conditions.[36] More interestingly, different in-plane orientations of overlayers were observed within a single domain of graphene, depending on adsorption site or lattice mismatch,[17] whose driving force is to minimize the interfacial energy[21] or dangling bond density of overlayer footprint.[33] The free-standing mono-atom-thick graphene levitated on hole-perforated silicon substrate yielded epitaxial InAs nanostructure/graphene heterostructures via vapor-phase vdW epitaxy.[21] All these works imply that graphene provides a strong interaction with overlayer so that determines the heteroepitaxial relation.

The use of van der Waals (vdW)-layered 2d-ALM substrates allows overlayer devices transferrable from the mother substrate to various others of interest through the exfoliation–stamping technique.[1,16,37] More importantly, such transferred devices exhibited no serious degradations in their electrical and electroluminescent properties even after experiencing the repetitive transfer procedures,[1,16] which validated the potential use of 2d-ALM substrates for transferrable, semi-transparent, and flexible device applications.[38,39] Among many types of

`

overlayer, the vertical wires on 2d-ALMs provide an ideal geometry enabling the use in a flexural and/or bent form without the device performance degradations because of spatially separated configuration of nanowire components.[24,38,40] Also, the site-selective growth[2,3] and heterogeneous growth of different functional-component vertical nanowires can be exploited to offer a platform toward heterogeneous integrated electronics and optoelectronics.[41-43] Meanwhile, ZnO is easily formed to have wire (or rod) morphology, due to the anisotropic surface formation energy,[44] and has been regarded as promising applications for high-performance laser, photodetector, and piezoelectric generator in a single crystalline form.[45-47] Importantly, ZnO nanowires were found to be vertically grown on graphene with a specific heteroepitaxial relationship.[13,32,38] Nonetheless, vdW or covalent epitaxy of semiconducting materials on 2d-ALMs have been severely hindered by lack of wafer-scale single crystalline 2d-ALM layers as substrates for industrial uses though a few reports of large scale growth of single-domain 2d-ALMs at wafer scale.[48,49]

The limitation of vdW or covalent epitaxy,[39,50] due to difficulty in large domain 2d-ALM substrate preparation, can be overcome by a new epitaxy technique reported by Kim *et al*.,[4] demonstrating homoepitaxial single crystalline layers of GaAs(001), InP(001), and GaP(001) over monolayer graphene (MLG) layers on GaAs(001), InP(001), and GaP(001) substrates, respectively, regardless of the graphene domain. Moreover, the heterojunction light-emitting diodes (LEDs) grown on these remote epitaxially grown (001)-overlayer revealed no degradation in electrical and electroluminescent performances even after exfoliation and the transfer of the LEDs on another substrates, and notably their performances were as good as high-quality LEDs prepared by conventional epitaxy based on covalent bindings between the overlayer and the substrate. This emerging epitaxy technique represented two important scientific findings, which are (i) the crystal structure and

`

orientation is copied from the underlying substrates to the overlayer across ultrathin 2d-ALMs, and (ii) the overlayer can be released and transferred onto an arbitrary substrate without quality degradation. Meanwhile, Chae *et al*. reported about the lattice transparency between the ZnO overlayer and substrate by means of wet chemical synthesis.[51] In particular, from as-grown ZnO polycrystallites/MLG/polycrystalline-ZnO substrate, the crystal structure and the orientation of overlayer ZnO polycrystallites were found to be the same locally with those of the underlying polycrystalline substrate, which signified that the lattice transparency is valid to copy the more complicated, heterogeneous crystal structures of substrates across MLG. Hence, it further needs to investigate the effect of crystal plane on lattice transparency (or remote epitaxy) for practical applications.

A key characteristic of remote epitaxy and lattice transparency of graphene is distance-dependence of interacting strength between the substrate and the overlayer across 2d-ALM, especially MLG. According to the work by Kim *et al*., the interaction between GaAs substrate and overgrown GaAs thin film weakens significantly in case of >0.9 nm gap formed by the presence of graphene.[4] To extend the realm of this technique, systematic studies of effects of (i) “physical gap” between substrate and overlayer and (ii) “substrate polarity (or crystal plane)” on interaction that results in the remote epitaxy and the lattice transparency are necessary for diverse materials and applications.[52]

In this paper, we report on hydrothermal remote homoepitaxy of the horizontal and vertical ZnO microrods (MRs) on graphene-coated *a*- and *c*-plane ZnO substrates, respectively. The density functional theory (DFT) calculations explore why/how the remote epitaxy occurred on graphene-coated ZnO substrate. The effects of substrate crystal plane and graphene thickness (or remote epitaxial gap) on interaction between overlayer and substrate (*i.e*., adhesion energy, interfacial structural change) are theoretically and experimentally

`

studied. The crystal structures of the remote homoepitaxial ZnO MRs/graphene/ZnO substrates are identified using a transmission electron microscopy. In addition, the weakly bound adhesion feature of graphene on the underlying substrate is utilized to transfer the remote homoepitaxial MRs overlayer via the simple exfoliation technique, which further enables regeneration of substrates, as well.

■ Experimental Section

Hydrothermal remote homoepitaxy and substrate preparation. In this study, we employed a typical synthesis condition for growing microsized ZnO rod arrays.[53] ZnO MRs were grown using a nutrient solution of equimolar zinc nitrate hexahydrate [$Zn(NO_3)_2 \cdot 6H_2O$, 25.0 mM] and hexamethylenetetramine [$C_6H_{12}N_4$, 25.0 mM] in deionized water at 95 °C for 4 hr in a teflon-lined autoclave (Fig. 1(a)). For the remote homoepitaxial substrate preparation, ZnO thin films with a thickness of 5–10 nm were formed by spin-coating a zinc acetate solution [$C_4H_6O_4Zn \cdot 2H_2O$, 5.0 mM in ethanol] at 2000 rpm on *r*-plane Al_2O_3 $(10\bar{1}2)$ and *c*-plane GaN (0001)/Al_2O_3 (0001) substrates in order to form *a*-plane ZnO $(11\bar{2}0)$ and *c*-plane ZnO (0001) substrates, followed by two-step annealing at 175 and 500 °C for 5 min in an air ambient. This spin-coating step was repeated at least thrice to form heteroepitaxial *a*- and *c*-ZnO substrates with a full coverage of the entire surface of *r*-Al_2O_3 and *c*-GaN/*c*-Al_2O_3 substrates, respectively. It is to be noted that the high-temperature annealing enabled the spin-coated thin ZnO layer to be heteroepitaxially crystallized on the original substrates of *c*-GaN and *r*-Al_2O_3.[54] For synthesis of the MLG, chemical vapor deposition (CVD) on 35 μm-thick copper foil (Nippon Mining & Metals) was employed, which yielded poly-domain MLG with a typical domain size of 5–20 μm.[55] Then, the MLG was transferred onto the ZnO substrates

`

by the poly(methyl–methacrylate)-supported etching–transfer technique.[56] For coating of multi-layer graphene on substrate, the MLG transfer process was repetitively performed onto the ZnO substrates, which yielded the graphene interlayers with accurate thickness. For bi-layer graphene (BLG) and tri-layer graphene (TLG), two and three MLG sheets were transferred onto the ZnO substrates. The graphene thickness was confirmed using the Raman spectroscopy (Fig. S1†).

Exfoliation and substrate regeneration. Prior to exfoliation of MR arrays, the gaps between MRs were filled by spin-coating of polyimide (PI). The PI layer was dried at 120 °C for 2 min, then thermally cured at 300 °C for 5 min. After thermal treatment, the PI-filled MRs overlayer was delaminated from the mother substrate via heat release tape-assisted peeling-off method. The tape was simply removed by heating the released layer at 190 °C. The procedures for exfoliation is schematically depicted in Fig 6(a). The exfoliated substrate was reused for the remote epitaxy by performing the MLG transfer and hydrothermal growth procedures described in the subsection above.

Characterizations. Surface morphologies of the samples were observed by FE-SEM (Hitachi S-4700). The graphene thickness was confirmed by Raman spectroscopic analysis (excitation laser with wavelength of 514 nm and power of 20 mW; Renishaw 2000). Crystal structures of the samples were examined using a HR-TEM (Jeol JEM-ARM 200F) observations and selected area electron diffraction (SAED) analyses. For the HR-TEM observations, samples were cross-sectionally milled with a 30 kV-accelerated beam of gallium ions using a focused ion beam machine (FEI Helios NanoLab^{TM}). The incidence electron beam was directed along the ZnO[0001] and $[10\bar{1}0]$ to determine the crystal structures of the remote homoepitaxial ZnO$[11\bar{2}0]$ and [0001] MRs, respectively.

`

Computational methods. The DFT calculations were performed within a generalized gradient approximation (GGA) for the exchange-correlation functionals,[57,58] and were implemented in the Vienna *ab*-initio simulation package (VASP).[59] The kinetic cutoff energy was set to 400 eV, and the projector augmented wave (PAW) potentials were employed to represent the electron–ion interactions.[60] For vdW corrections, Grimme's DFT-D3 method based on a semi-empirical GGA-type theory was adopted.[61] For remote homoepitaxial *a*-ZnO/graphene/*a*-ZnO, (4 × 3) surface unit cell of ZnO ($11\bar{2}0$) and the (5 × 4) rectangular unit cell of graphene were calculated using lattice mismatches of 2.57 and 1.39% in *x*- and *y*-axes, respectively, while the (3 × 3) surface unit cell of oxygen-terminated ZnO (0001) and the (4 × 4) rhombic unit cell of graphene were calculated using lattice mismatch of 0.91% between them for remote epitaxial *c*-ZnO/graphene/*c*-ZnO. Regarding the Brillouin zone integration, (2 × 3 × 1) grid for *a*-ZnO/graphene/*a*-ZnO and (3 × 3 × 1) grid for *c*-ZnO/graphene/*c*-ZnO were used in the Gamma centred scheme. The atomic configurations were fully optimized as long as the Hellmann–Feynman forces became less than 0.02 eV $Å^{-1}$. The charge density difference (ΔCD) was determined by the expression $\Delta CD_{graphene/ZnO} = n_{graphene/ZnO} - (n_{graphene} + n_{ZnO})$, where $n_{graphene/ZnO}$, $n_{graphene}$, and n_{ZnO} are charge densities of graphene/ZnO, graphene, and ZnO, respectively. For the graphene-coated ZnO substrates, the ΔCD of the remote homoepitaxial heterointerfaces was also calculated using $\Delta CD_{ZnO/graphene/ZnO} = n_{ZnO/graphene/ZnO} - (n_{ZnO(overlayer)} + n_{graphene/ZnO})$, where $n_{ZnO/graphene/ZnO}$, $n_{ZnO(overlayer)}$, and $n_{graphene/ZnO}$ are charge densities of ZnO/graphene/ZnO, ZnO overlayer, and graphene/ZnO substrate, respectively.

■ Results and Discussion

`

As depicted in Fig. 1(a), remote homoepitaxy was performed via hydrothermal growth of ZnO MRs on graphene-coated *a*- and *c*- plane ZnO substrates. Figs. 1(b) and (c) schematically represent the surface morphologies of remote homoepitaxial ZnO MR arrays grown on MLG-coated *a*- and *c*-ZnO substrates, respectively. Intriguingly, although ZnO MRs were grown on the same smooth, clean MLG surface (insets in Figs. 1(d) and (e)) under the same hydrothermal growth conditions, even in the same batch, two templates of the MLG/*a*-ZnO and the MLG/*c*-ZnO yielded two different overlayer morphologies of horizontally and vertically aligned MR arrays, respectively (Figs. 1(d) and (e)). Noticeably, these MRs were found to be well aligned with good in-plane ordering of unidirectional horizontal arrays (Fig. 1(d)) and a uniform six-fold rotational alignment of vertical MR sidewall $\{1\bar{1}00\}$ facets (indicated with arrows in Fig. 1(e)) by plan-view field-emission scanning electron microscope (FE-SEM) observations. This suggests the existence of specific epitaxial relationships between MRs and ZnO substrates.

The cross-sectional FE-SEM image of a single horizontal ZnO MR, shown at the bottom panel of Fig. 1(d), clearly exhibits a lying-down morphology of the prismatic rod with facets of $\{1\bar{1}00\}$ *m*-planes (red and green colored) and (0001) *c*-plane (blue colored) of wurtzite, whose body is cut in half along the *a*-plane, parallel to the substrate surface. These morphological features were identically observed from other horizontal MRs as well. As displayed in Fig. 1(e), MR arrays grown on MLG/*c*-ZnO show the vertical alignment without exception.

If the MLG surface as a seed layer offered the epitaxial relationship, the homogeneous alignments of MR arrays could not be achieved in such a long range over the entire substrate area because the mean domain size of the CVD-grown graphene is typically a few μm. Hence, such long-range morphological ordering of as-grown MRs shown in Fig. 2 is tentatively

`

associated with single crystallinity of the ZnO substrates even though the poly-domain graphene is covered on the substrates. It is worth noting that the MLG was not damaged after the hydrothermal growth of the ZnO because of the low temperature and the mild growth condition, which was confirmed by the Raman spectroscopic analysis (Fig. S2†).

Crystal structures and epitaxial relationships of the ZnO MR/MLG/ZnO substrate were examined using a high-resolution transmission electron microscope (HR-TEM). Fig. 3(a) displays the cross-sectional HR-TEM image taken around the heterointerfaces of the horizontal ZnO MR/MLG/*a*-ZnO (on *r*-Al_2O_3), which showed the structural discontinuity, as indicated by red arrows, because of the MLG existence between the *a*-ZnO overlayer and the substrate. Two lattice images of the overlayer and the substrate in Fig. 3(b) clearly demonstrate the identical lattice arrangements of the ZnO MR overlayer and the substrate. Considering the lattice constants of ZnO ($a = b = 3.249$ Å; $c = 5.206$ Å for wurtzite), those lattice images represent a remote homoepitaxial relationship of $(11\bar{2}0)[0001]_{\text{overlayer}} \| (11\bar{2}0)[0001]_{\text{substrate}}$ across the MLG. Also, the SAED patterns also identified the aforementioned remote homoepitaxial relationship (Fig. 3(c)), without no other irregular diffraction spots caused from the ZnO. This indicates a single crystallinity of the remote homoepitaxial *a*-ZnO overlayer/*a*-ZnO substrate. The diffraction patterns also corroborate that the *a*-ZnO substrate was heteroepitaxially grown on *r*-Al_2O_3 with a relationship of $(11\bar{2}0)[0001]_{\text{ZnO substrate}} \| (1\bar{1}02)[\bar{1}101]_{r\text{-sapphire}}$.

In Figs. 3(d) and (e), the same *c*-axial crystallographic orientations of the wurtzite ZnO overlayer and substrate are displayed, which were taken from the vertical ZnO MR/MLG/*c*-ZnO (on *c*-GaN). The lattice orientations of the *c*-ZnO overlayer and substrate were found to be well matched and aligned, which indicated the remote homoepitaxial $(0001)[10\bar{1}$

`

$0]_{overlayer} \| (0001)[10\bar{1}0]_{substrate}$ relationship. The interplanar spacings between adjacent lattice planes in both the ZnO overlayer and substrate were measured to be 2.59 Å that corresponds to the *d*-spacing of ZnO (0002). As shown in Fig. 3(f), the SAED patterns reveal the epitaxial $(0001)[10\bar{1}0]_{MR} \| (0001)[10\bar{1}0]_{ZnO\ substrate} \| (0001)[10\bar{1}0]_{GaN}$ relationship, and noticeably the remote homoepitaxial relationship was well maintained even with the use of thicker graphene interlayers of BLG or TLG (Fig. S3†).

It is well known that the CVD-grown MLG has many defects, such as vacancy and small opening, on which possibly provokes opening-mediated nucleation directly from ZnO substrate, followed by epitaxial lateral overgrowth (ELOG). However, in the cross-sectional TEM analysis, it was difficult to observe the evidence of opening-assisted growth at the center of MR footprint from several MR TEM samples (Fig. S3†). Furthermore, to avoid such opening-mediated ELOG, we employed the BLG and TLG interlayers prepared by repeating the MLG transfer process, as schematically depicted in Fig. S4†. Thus, it is surmised that this technique guarantees the use of nearly opening-free BLG and TLG interlayer for remote epitaxy, rather than the transfer of CVD-grown BLG and TLG.

The DFT calculations were conducted to explore how/why the remote epitaxy of the ZnO overlayer was made possible across graphene layers. The stable molecular structures were simulated, and charge transfer (or redistribution) at the heterointerface was estimated by calculating ΔCD for the substrate and remote homoepitaxial structures. The left panel of Fig. 4(a) shows the calculated structure of MLG adheres to an *a*-ZnO substrate with the equilibrium vdW gap of 2.95 Å and adhesion energy of –21.5 meV $Å^{-2}$ for the MLG/*a*-ZnO substrate before the overlayer growth, and the charge transfer mostly occurs at the graphene/*a*-ZnO interface. Though the electron (e^-) accumulation and depletion appear alternately along the MLG side within the non-covalent binding gap, e^- depletion is slightly

`

predominant around the MLG and the surface of MLG shows e^- depleted surface. Only a small amount of e^- accumulation remains at the *a*-ZnO substrate. Hence, as depicted in inset of Fig. 4(a), the charge redistribution at the vdW binding interface possibly makes electric dipole (or bond dipole) with a vertical directional component. Intriguingly, the slight lattice buckling was simulated on both sides. In particular, interfacial oxygen ions protrude toward the graphene, which possibly breaks the perfect non-polar symmetry of the wurtzite *a*-plane. As a result, the e^- depletion becomes slightly dominant at the substrate side with a net positive charge, which develops electric dipoles with a normal direction component (inset of Fig. 4(a)). This leads to the diffuse-in and adhesion of precursor adatoms, followed by nucleation–epitaxy.

The right panel of Fig. 4(a) shows the remote homoepitaxial *a*-ZnO/MLG/*a*-ZnO heterointerfaces, displaying that the ΔCD appears at the overlayer/MLG interface, tentatively due to charge transfer. Such charge redistribution makes the strong bond dipoles with vertical direction component at the overlayer/MLG interface, as depicted in dot-line box of right panel in Fig. 4(a). The equilibrium spacings of the overlayer–MLG and MLG–substrate are 2.89 and 2.88 Å, respectively, and the adhesion energy of overlayer–(MLG-coated substrate) was estimated to be –24.5 meV $Å^{-2}$. It should be noted that the spacing of the MLG–substrate becomes smaller with decreased adhesion energy after the remote homoepitaxy, presumably due to the strong attraction between the overlayer and substrate across graphene.

Meanwhile, in the MLG/*c*-ZnO substrate (left panel of Fig. 4(b)), the e^- depletion dominantly appears along the adhered MLG side while electrons are accumulated on the *c*-ZnO substrate, which lead to formation of vertical electric dipoles. The adhesion energy of MLG on *c*-ZnO was –31.3 meV $Å^{-2}$ with a gap distance of 3.12 Å. After the growth of the overlayer (right panel of Fig. 4(b)), the ΔCD additionally appears at the overlayer/MLG

`

interface (dot-line box), implying that the attraction from the substrate transferred to the overlayer across graphene. For the remote epitaxial structure, the spacings of the overlayer–MLG and MLG–substrate are calculated to be 2.69 and 2.78 Å, respectively, and the adhesion energy of the overlayer to MLG is –52.0 meV $Å^{-2}$. We noted that the spacing of the MLG–*c*-ZnO substrate is significantly reduced from 3.12 to 2.78 Å after remote epitaxy, due to the strong electrostatic attraction carried through the vertical dipoles between the overlayer and substrate. The smaller calculated gap distance of 5.47 Å between overlayer and substrate in the *c*-axial remote homoepitaxial structure than that in the *a*-axial one (5.77 Å) support the crucial role of substrate polarity in more energetically stable remote homoepitaxial structures with a substantial energy saving and stronger attraction between overlayer and substrates.

The remote epitaxial *c*-ZnO/BLG/*c*-ZnO structures were further calculated to examine the effect of the graphene thickness (or remote epitaxial gap) on ΔCD and the heterointerfacial structure. Fig. 4(c) exhibits that the top of the *c*-ZnO substrate and the surface of the BLG are oppositely charged before remote homoepitaxy, and in between them charge accumulation and depletion regions alternately forms, which results in formation of vertical dipoles. After remote epitaxy, the ΔCD predominantly appears between the top of the BLG and the bottom of the *c*-ZnO with adhesion energy of –32.3 meV $Å^{-2}$, whose absolute value is much smaller than that of the *c*-ZnO on MLG/*c*-ZnO, because of increased gap between the overlayer and substrate. Thus, the use of thicker graphene reduces the adhesion of overlayer due to the wider physical gap between the overlayer and substrate. The DFT-calculated results imply that the amount of net charge difference (or the amount of charge transfer) along the *z*-axis plays an important role in determining both the equilibrium distance and the adhesion energy of the overlayer–graphene (see also Fig. S5† for charge redistribution at isosurface levels of ±0.001 e/$bohr^3$). In practice, the use of polar *c*-ZnO

`

and/or thinner graphene (or remote epitaxial gap) is surmised to induce a stronger attraction between substrate and adatoms adhered onto graphene surface, which possibly facilitates the enhanced nucleation of the overlayer.[62]

In this regard, the impact of the remote epitaxial gap was empirically investigated by growing MRs on graphene-coated ZnO substrates with different graphene thicknesses (e.g., MLG, BLG, and TLG-coated substrates). The growth of MRs enabled to study the effect of graphene thickness on the remote epitaxy by counting the growth density. Fig. 5 displays the number density of remote epitaxial MRs plotted as a function of graphene thickness. Overall, the MR number density was decreased with increase of graphene thickness because of the dipole momentum damping as a function of remote epitaxial gap. For instance, when using an *a*-ZnO substrate (Fig. 5(a)), the number density was reduced from 9.8×10^3 to 1.4×10^3 mm^{-2} as increasing the graphene thickness from MLG to TLG; for the use of *c*-ZnO substrate (Fig. 5(b)), 1.7×10^5 to 2.2×10^4 mm^{-2}. It should be also noted that the use of the *c*-ZnO substrate yielded a much higher MR number density than the *a*-ZnO under the same gap conditions. This result identifies that a higher field strength with a polar substrate and/or a narrower gap is crucial to form remote epitaxial nano/microstructures of higher density.

According to the work by Kong *et al*.,[52] the remote epitaxy of single-crystalline wurtzite *c*-plane GaN film was successful across BLG, but TLG disturbed the remote epitaxy so that polycrystalline GaN film was produced due to field attenuation through the thick graphene. In this work, the remote epitaxy of ZnO was possible across TLG, but the use of graphene thicker than TLG yielded randomly oriented MR arrays without the in-plane ordering. Because many physical properties of GaN and ZnO are quite similar (*i.e*., crystal structure, lattice constant, bandgap, *etc*.), it seems plausible that the limit of graphene thickness for the remote epitaxy of ZnO must be BLG equally. However, as interpreted by Kong *et al*., the

`

difference of atomic bonding feature determines the distance of remote epitaxy,[52] and more ionicity of ZnO must be the reason that the remote atomic interacting field penetrated the TLG so that the adatom alignment was guided with respect to the substrate lattice alignment. It is to be noted that this was also occurred for the use of apolar ZnO substrate because the apolar crystal symmetry of substrate was broken by the lattice buckling near the interface. We believe that our results, as II–VI remote homoepitaxy, contribute to provide a piece of experimental information upon the pioneering work across the periodic table.[52]

Exfoliation of the remote epitaxial ZnO MRs overlayer was carried out to adopt the ability of graphene to be readily released from substrate, because of the weakly bound vdW bonds to the mother substrate surface. We particularly attempted the release of vertical MRs with a high aspect ratio of ~6. For the overlayer exfoliation, PI was spin-coated between MRs. The PI-supported MRs overlayer was then delaminated from the mother substrate using the heat release tape that can be removed by heating on a hot plate. A series of schematics and photographs in Fig. 6(a) exhibits the exfoliation procedures and the corresponding resultant products, respectively. The SEM image of Fig. 6(b), taken from released side of PI-coated MR arrays, shows a smooth bottom finish of *c*-ZnO MRs. Furthermore, the surface of the remained *c*-ZnO substrate after the release was found to be quite smooth and clean (inset of Fig. 6(b)). This signifies that the bottom of ZnO MRs overlayer was completely released from the mother substrate.

The location of graphene after exfoliation was confirmed using Raman spectroscopy (Fig. 6(c)). Before the exfoliation, the ZnO MRs/graphene/ZnO substrate exhibited graphene-associated peaks, which are D, G, and 2D, at 1347, 1572, and 2669 cm^{-1}, respectively. However, after exfoliation, these peaks were not observed on the mother substrate but on the released backside of the PI-coated MRs overlayer. This indicates that the graphene was

`

completely removed together with the MRs overlayer from the mother substrate using the simple mechanical tape-release technique. According to the work by Kim *et al*., the graphene interlayer remains on the substrate after release of a thin film overlayer,[4] which is different from our result that the graphene is transferred in conjunction with the overlayer. We surmise that either the use of a sticky, adhesive gap filler PI or a stronger adhesion between the graphene and the overlayer (Fig. 4) facilitated the delamination of the overlayer/graphene from the mother substrate. Note that the exfoliation was not successful when MLG with many defects is used as the gap interlayer because of strong direct ionic bonds between MRs and substrate through the MLG-free opening defects.

The successful exfoliation was extended to the regeneration of the used ZnO substrate. The mother substrates after the exfoliation were reused by repeating the procedures of graphene transfer and hydrothermal growth of ZnO MRs which are shown in Fig. 1(a). Fig. 7 displays that the reuse of mother substrates with MLG interlayer produced the remote homoepitaxial MR arrays whose morphologies and number densities (within a deviation of ±10%) are almost same with those grown on the virgin substrates. For the use of BLG and TLG interlayers, the reused mother substrates yielded well aligned MR arrays as well (Fig. S6†). This indicated that the substrates can be reliably reused for cost-saving production of the transferable MR arrays.

■ Conclusion

In summary, we have demonstrated the remote homoepitaxy of ZnO MRs using graphene-coated ZnO substrates with different remote oepitaxial gaps and substrate crystal planes. Both the *a*- and *c*-plane ZnO substrates, which correspond to apolar and polar

`

surfaces, respectively, yielded horizontal and vertical MR arrays with homogeneous in-plane alignment, because of homoepitaxial relationship across graphene. As increasing the remote epitaxial gap with use of thicker graphene, the number density of MRs was significantly decreased, and polar substrate resulted in higher density MR arrays. These experimental results corroborate our argument that stronger electric dipole momentum along *z*-direction from the substrate side can be well transferred through thinner graphene, which eventually attracts more adatoms for higher density formation of MRs. According to DFT calculations, the electric dipole (or potential field) induced via charge redistribution by junction of graphene/substrate played an important role for remote homoepitaxy. Strong attraction between overlayer and substrate resulted in decreased interplanar spacings with substantial adhesion energy savings. Moreover, the attraction was calculated to be strongly affected by both the gap distance and substrate crystal plane, which elucidates why polar and smaller gaps produced higher density MR arrays. We surmise that the vdW heterointerface and graphene without permanent dipoles enabled the penetration of induced dipoles formed at the graphene/substrate junction across graphene layers. Our complementary theoretical and experimental results provide fundamental insights for understanding the ability of graphene layers that penetrate the electric dipole momentum for remote homoepitaxy. More importantly, we showed that the use of multilayer graphene (*e.g.*, BLG and TLG) is possible to obtain remote homoepitaxial MR arrays on both polar and apolar substrates for the first time. For practical applications, the vdW binding of graphene to the substrate presented important implications for release of MRs overlayer and reuse of substrates. Hence, we anticipate that this promising method could be readily applied to fabricate more materials and diverse devices that are transferrable from regenerated substrates on demands.

`

Conflicts of interest

There are no conflicts of interest to declare.

Acknowledgement

This research was financially supported by the Basic Science Research Programs (NRF-2016R1D1A1B03931518; NRF-2015R1A2A2A05050829; NRF-2017R1A2B2010123), Priority Research Center Program (2010-0020207) and International Research Center Program (2018K1A4A3A01064272) through the NRF of Korea. The authors gratefully acknowledge financial support of the KIAT through the International Cooperative R&D program (N0001819). This work was supported by Laboratory Directed Research and Development and CINT, a U.S. Department of Energy, office of Basic Energy Sciences User Facility at Los Alamos National Laboratory (Contract DE-AC52-06NA25396) and Sandia National Laboratories (Contract DE-AC04-94AL85000).

■ REFERENCES

1. K. Chung, C. H. Lee and G. C. Yi, *Science*, 2010, **330**, 655–657.
2. Y. J. Hong, C. H. Lee, A. Yoon, M. Kim, H. K. Seong, H. J. Chung, C. Sone, Y. J. Park and G. C. Yi, *Adv. Mater.*, 2011, **23**, 3284–3288.
3. K. Tomioka, M. Yoshimura and T. Fukui, *Nature*, 2012, **488**, 189–192.
4. Y. Kim, S. S. Cruz, K. Lee, B. O. Alawode, C. Choi, Y. Song, J. M. Johnson, C. Heidelberger, W. Kong, S. Choi, K. Qiao, I. Almansouri, E. A. Fitzgerald, J. Kong, A. M. Kolpak, J. Hwang and J. Kim, *Nature*, 2017, **544**, 340–343.
5. S. Gazibegovic, D. Car, H. Zhang, S. C. Balk, J. A. Logan, M. W. A. de Moor, M. C. Cassidy, R. Schmits, D. Xu, G. Z. Wang, P. Krogstrup, R. Veld, K. Zuo, Y. Vos, J. Shen, D. Bouman, B. S. Hojaei, D. Pennachio, J. S. Lee, P. J. van Veldhoven, S. Koelling, M. A. Verheijen, L. P. Kouwenhoven, C. J. Palmstrom and E. Bakkers, *Nature*, 2017, **548**, 434–438.
6. J. E. Ayers, *Heteroepitaxy of semiconductor: Theory, Growth, and Characterization*, CRC Press, Boca Raton, FL, Boca Raton, FL, 1st edn., 2007.

`

7. W. S. Wong, T. Sands, N. W. Cheung, M. Kneissl, D. P. Bour, P. Mei, L. T. Romano and N. M. Johnson, *Appl. Phys. Lett.*, 1999, **75**, 1360–1362.
8. J. Yoon, S. Jo, I. S. Chun, I. Jung, H. S. Kim, M. Meitl, E. Menard, X. L. Li, J. J. Coleman, U. Paik and J. A. Rogers, *Nature*, 2010, **465**, 329–333.
9. C. W. Cheng, K. T. Shiu, N. Li, S. J. Han, L. Shi and D. K. Sadana, *Nat. Commun.*, 2013, **4**, 1577.
10. J. H. Cheng, Y. S. Wu, W. C. Peng and H. Ouyang, *J. Electrochem. Soc.*, 2009, **156**, H640–H643.
11. M. H. Doan, S. Kim, J. J. Lee, H. Lim, F. Rotermund and K. Kim, *AIP Adv.*, 2012, **2**, 022122.
12. J. M. Lee, Y. B. Pyun, J. Yi, J. W. Choung and W. I. Park, *J. Phys. Chem. C*, 2009, **113**, 19134–19138.
13. Y. J. Kim, J. H. Lee and G. C. Yi, *Appl. Phys. Lett.*, 2009, **95**, 213101.
14. Y. J. Hong and T. Fukui, *ACS Nano*, 2011, **5**, 7576–7584.
15. Y. J. Hong, W. H. Lee, Y. P. Wu, R. S. Ruoff and T. Fukui, *Nano Lett.*, 2012, **12**, 1431–1436.
16. Y. Kobayashi, K. Kumakura, T. Akasaka and T. Makimoto, *Nature*, 2012, **484**, 223–227.
17. A. M. Munshi, D. L. Dheeraj, V. T. Fauske, D. C. Kim, A. T. J. van Helvoort, B. O. Fimland and H. Weman, *Nano Lett.*, 2012, **12**, 4570–4576.
18. K. Chung, S. I. Park, H. Baek, J. S. Chung and G. C. Yi, *Npg Asia Mater*, 2012, **4**, e24.
19. P. K. Mohseni, A. Behnam, J. D. Wood, C. D. English, J. W. Lyding, E. Pop and X. L. Li, *Nano Lett.*, 2013, **13**, 1153–1161.
20. A. M. Munshi and H. Weman, *Phys. Status Solidi RRL*, 2013, **7**, 713–726.
21. Y. J. Hong, J. W. Yang, W. H. Lee, R. S. Ruoff, K. S. Kim and T. Fukui, *Adv. Mater.*, 2013, **25**, 6847–6853.
22. J. Wallentin, D. Kriegner, J. Stangl and M. T. Borgstrom, *Nano Lett.*, 2014, **14**, 1707–1713.
23. P. K. Mohseni, A. Behnam, J. D. Wood, X. Zhao, K. J. Yu, N. C. Wang, A. Rockett, J. A. Rogers, J. W. Lyding, E. Pop and X. L. Li, *Adv. Mater.*, 2014, **26**, 3755–3760.
24. K. Chung, H. Beak, Y. Tchoe, H. Oh, H. Yoo, M. Kim and G. C. Yi, *APL Mater.*, 2014, **2**, 092512.
25. A. A. Balandin, S. Ghosh, W. Z. Bao, I. Calizo, D. Teweldebrhan, F. Miao and C. N. Lau, *Nano Lett.*, 2008, **8**, 902–907.
26. C. Lee, X. D. Wei, J. W. Kysar and J. Hone, *Science*, 2008, **321**, 385–388.
27. D. C. Wei, Y. Q. Liu, Y. Wang, H. L. Zhang, L. P. Huang and G. Yu, *Nano Lett.*, 2009, **9**, 1752–1758.
28. X. S. Li, W. W. Cai, J. H. An, S. Kim, J. Nah, D. X. Yang, R. Piner, A. Velamakanni, I. Jung, E. Tutuc, S. K. Banerjee, L. Colombo and R. S. Ruoff, *Science*, 2009, **324**, 1312–1314.
29. S. Bae, H. Kim, Y. Lee, X. F. Xu, J. S. Park, Y. Zheng, J. Balakrishnan, T. Lei, H. R. Kim, Y. I. Song, Y. J. Kim, K. S. Kim, B. Ozyilmaz, J. H. Ahn, B. H. Hong and S. Iijima, *Nat. Nanotech.*, 2010, **5**, 574–578.
30. D. Mohanty, W. Y. Xie, Y. P. Wang, Z. H. Lu, J. Shi, S. B. Zhang, G. C. Wang, T. M. Lu and I. B. Bhat, *Appl. Phys. Lett.*, 2016, **109**, 143109.
31. X. Sun, Z. H. Lu, W. Y. Xie, Y. P. Wang, J. Shi, S. B. Zhang, M. A. Washington and T. M. Lu, *Appl. Phys. Lett.*, 2017, **110**, 153104.

`

32. Y. J. Kim, H. Yoo, C. H. Lee, J. B. Park, H. Baek, M. Kim and G. C. Yi, *Adv. Mater.*, 2012, **24**, 5565–5569.
33. H. K. Hong, J. Jo, D. Hwang, J. Lee, N. Y. Kim, S. Son, J. H. Kirn, M. J. Jin, Y. C. Jun, R. Erni, S. K. Kwak, J. W. Yoo and Z. Lee, *Nano Lett.*, 2017, **17**, 120–127.
34. J. E. Choi, J. Yoo, D. Lee, Y. J. Hong and T. Fukui, *Appl. Phys. Lett.*, 2018, **112**, 142101.
35. V. Kumaresan, L. Largeau, A. Madouri, F. Glas, H. Z. Zhang, F. Oehler, A. Cavanna, A. Babichev, L. Travers, N. Gogneau, M. Tchernycheva and J. C. Harmand, *Nano Lett.*, 2016, **16**, 4895–4902.
36. E. Mataev, S. K. Rastogi, A. Madhusudan, J. Bone, N. Lamprinakos, Y. Picard and T. Cohen-Karni, *Nano Lett.*, 2016, **16**, 5267–5272.
37. J. Kim, C. Bayram, H. Park, C. W. Cheng, C. Dimitrakopoulos, J. A. Ott, K. B. Reuter, S. W. Bedell and D. K. Sadana, *Nat. Commun.*, 2014, **5**, 4836.
38. C. H. Lee, Y. J. Kim, Y. J. Hong, S. R. Jeon, S. Bae, B. H. Hong and G. C. Yi, *Adv. Mater.*, 2011, **23**, 4614–4619.
39. Y. J. Hong and C. H. Lee, in *Semiconductor Nanowires I: Growth and Theory*, eds. A. F. I. Morral, S. A. Dayeh and C. Jagadish, Academic Press, Burlington, 2015, vol. 93, ch. 3, pp. 125–172.
40. D. Choi, M. Y. Choi, W. M. Choi, H. J. Shin, H. K. Park, J. S. Seo, J. Park, S. M. Yoon, S. J. Chae, Y. H. Lee, S. W. Kim, J. Y. Choi, S. Y. Lee and J. M. Kim, *Adv. Mater.*, 2010, **22**, 2187–2192.
41. H. Sekiguchi, K. Kishino and A. Kikuchi, *Appl. Phys. Lett.*, 2010, **96**, 231104.
42. R. Wang, H. P. T. Nguyen, A. T. Connie, J. Lee, I. Shih and Z. Mi, *Opt. Express*, 2014, **22**, A1768–A1775.
43. Y. H. Ra, R. Wang, W. S. Y., M. Djavid, S. M. Sadaf, J. Lee, G. A. Botton and Z. Mi, *Nano Lett.*, 2016, **16**, 4608–4615.
44. Y. J. Hong, J. Yoo, Y. J. Doh, S. H. Kang, K. J. Kong, M. Kim, D. R. Lee, K. H. Oh and G. C. Yi, *J. Mater. Chem.*, 2009, **19**, 941–947.
45. M. H. Huang, S. Mao, H. Feick, H. Q. Yan, Y. Y. Wu, H. Kind, E. Weber, R. Russo and P. D. Yang, *Science*, 2001, **292**, 1897–1899.
46. C. Soci, A. Zhang, B. Xiang, S. A. Dayeh, D. P. R. Aplin, J. Park, X. Y. Bao, Y. H. Lo and D. Wang, *Nano Lett.*, 2007, **7**, 1003–1009.
47. Z. L. Wang and J. H. Song, *Science*, 2006, **312**, 242–246.
48. J. H. Lee, E. K. Lee, W. J. Joo, Y. Jang, B. S. Kim, J. Y. Lim, S. H. Choi, S. J. Ahn, J. R. Ahn, M. H. Park, C. W. Yang, B. L. Choi, S. W. Hwang and D. Whang, *Science*, 2014, **344**, 286–289.
49. X. Z. Xu, Z. H. Zhang, J. C. Dong, D. Yi, J. J. Niu, M. H. Wu, L. Lin, R. K. Yin, M. Q. Li, J. Y. Zhou, S. X. Wang, J. L. Sun, X. J. Duan, P. Gao, Y. Jiang, X. S. Wu, H. L. Peng, R. S. Ruoff, Z. F. Liu, D. P. Yu, E. G. Wang, F. Ding and K. H. Liu, *Sci. Bull.*, 2017, **62**, 1074–1080.
50. H. Yoo, K. Chung, Y. S. Choi, C. S. Kang, K. H. Oh, M. Kim and G. C. Yi, *Adv. Mater.*, 2012, **24**, 515–518.
51. S. Chae, S. H. Jang, W. J. Choi, Y. S. Kim, H. J. Chang, T. I. Lee and J. O. Lee, *Nano Lett.*, 2017, **17**, 1711–1718.
52. W. Kong, H. S. Li, K. Qiao, Y. Kim, K. Lee, Y. F. Nie, D. Lee, T. Osadchy, R. J. Molnar, D. K. Gaskill, R. L. Myers-Ward, K. M. Daniels, Y. W. Zhang, S. Sundram, Y. Yu, S. H. Bae, S. Rajan, Y. Shao-Horn, K. Cho, A. Ougazzaden, J. C. Grossman and J. Kim, *Nat. Mater.*, 2018, **17**, 999–1004.

`

53. J. Jeong, J. E. Choi, Y. J. Kim, S. Hwang, S. K. Kim, J. K. Kim, H. Y. Jeong and Y. J. Hong, *Appl. Phys. Lett.*, 2016, **109**, 22–26.
54. L. E. Greene, M. Law, D. H. Tan, M. Montano, J. Goldberger, G. Somorjai and P. D. Yang, *Nano Lett.*, 2005, **5**, 1231–1236.
55. D. S. Choi, K. S. Kim, H. Kim, Y. Kim, T. Kim, S. H. Rhy, C. M. Yang, D. H. Yoon and W. S. Yang, *ACS Appl. Mater. Interfaces*, 2014, **6**, 19574–19578.
56. K. S. Kim, Y. Zhao, H. Jang, S. Y. Lee, J. M. Kim, K. S. Kim, J. H. Ahn, P. Kim, J. Y. Choi and B. H. Hong, *Nature*, 2009, **457**, 706–710.
57. W. Kohn and L. J. Sham, *Phys. Rev.*, 1965, **140**, A1133–A1138.
58. J. P. Perdew, K. Burke and M. Ernzerhof, *Phys. Rev. Lett.*, 1996, **77**, 3865–3868.
59. G. Kresse and J. Furthmuller, *Phys. Rev. B*, 1996, **54**, 11169–11186.
60. G. Kresse and D. Joubert, *Phys. Rev. B*, 1999, **59**, 1758–1775.
61. S. Grimme, J. Antony, S. Ehrlich and H. Krieg, *J. Chem. Phys.*, 2010, **132**, 154104.
62. J. Yoo, T. Ahmed, R. J. Chen, A. P. Chen, Y. H. Kim, K. C. Kwon, C. W. Park, H. S. Kang, H. W. Jang, Y. J. Hong, W. S. Yang and C. H. Lee, *Nanoscale*, 2018, **10**, 5689–5694.

`

Figures and captions

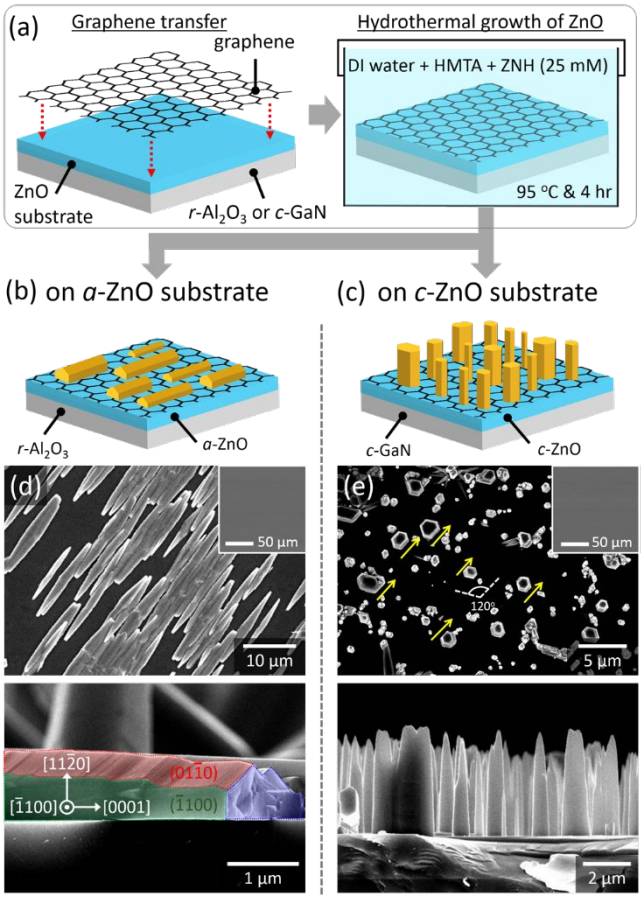

Fig. 1. Remote homoepitaxial growth of ZnO MRs on graphene-coated ZnO substrates. (a) Schematic illustration depicting the procedures for hydrothermal remote homoepitaxy. Illustrations of ZnO MRs remote-epitaxially grown on (b) *a*-ZnO and (c) *c*-ZnO substrates across MLG. Top-view (upper panel) and cross-sectional (bottom panel) SEM images of ZnO MRs grown on MLG-coated (d) *a*-ZnO and (e) *c*-ZnO substrates. Insets in upper panels of (d) and (e) are plan-view SEM images of MLG-coated *a*- and *c*-ZnO substrates, respectively, before overlayer growth. The bottom image in (d) is false-colored to represent facets of (0001), ($\bar{1}$100), and (01$\bar{1}$0) with blue, green, and red, respectively. HMTA and ZNH in (a) denote hexamethylenetetramine and zinc nitrate hexahydrate, respectively.

`

1

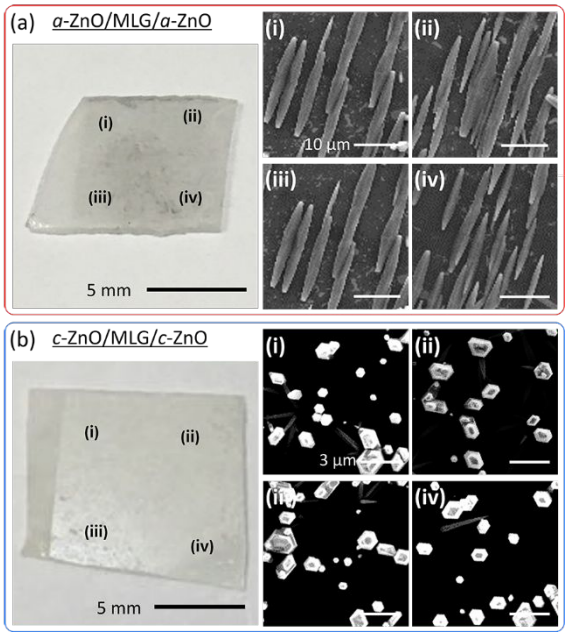

2

3 **Fig. 2**. Long-range morphological ordering of remote homoepitaxial ZnO MR arrays grown
4 on MLG-coated (a) *a*-ZnO and (b) *c*-ZnO substrate. Left panel is photograph of substrate with
5 a thumbnail size, and right four panels are a series of plan-view SEM images (right) obtained
6 from (i)–(iv) locations marked in the left photograph. For SEM observations, the sample
7 stage was only translationally moved without rotating motion to corroborate the in-plane
8 alignments of MR arrays.

9

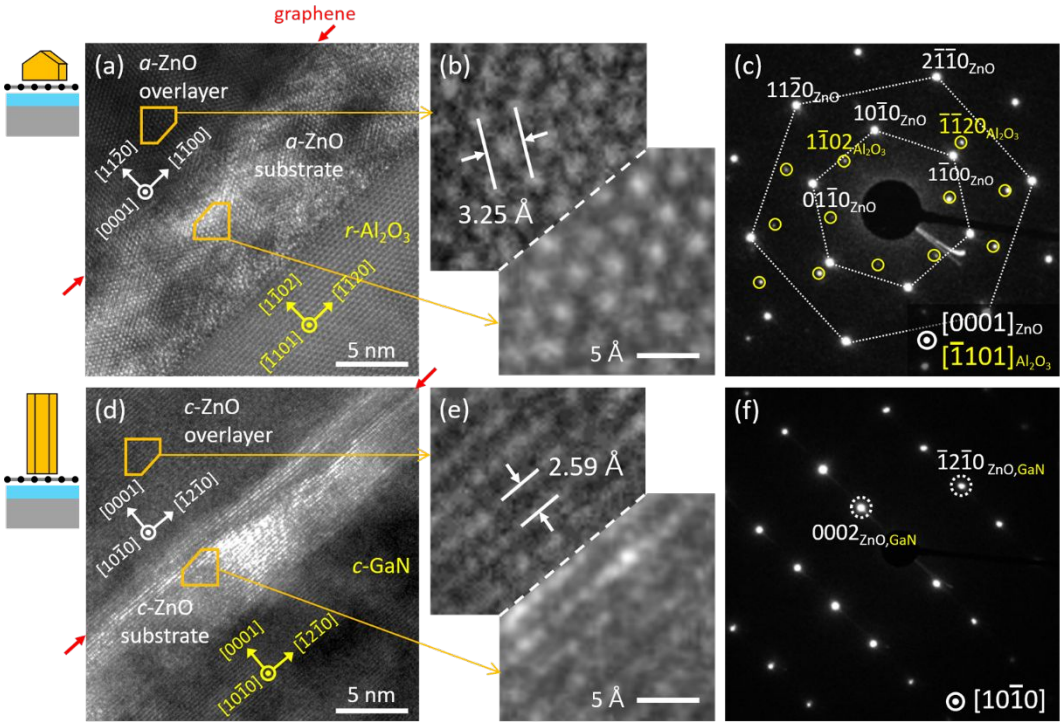

Fig. 3. Cross-sectional TEM analyses of remote homoepitaxial ZnO MRs/MLG/ZnO substrate. (a) HR-TEM image of horizontal ZnO MR/MLG/*a*-ZnO substrate. (b) The corresponding high-magnification lattice images enlarged from boxed areas of (a). (c) SAED patterns obtained from image of (a). (d) HR-TEM image of vertical ZnO MR/MLG/*c*-ZnO substrate. (e) The corresponding high-magnification lattice images enlarged from the boxed areas of (d). (f) SAED patterns obtained from image (d). The diffraction patterns of (c) and (f) demonstrate the homoepitaxial relationship between the ZnO MR overlayer and substrate across MLG.

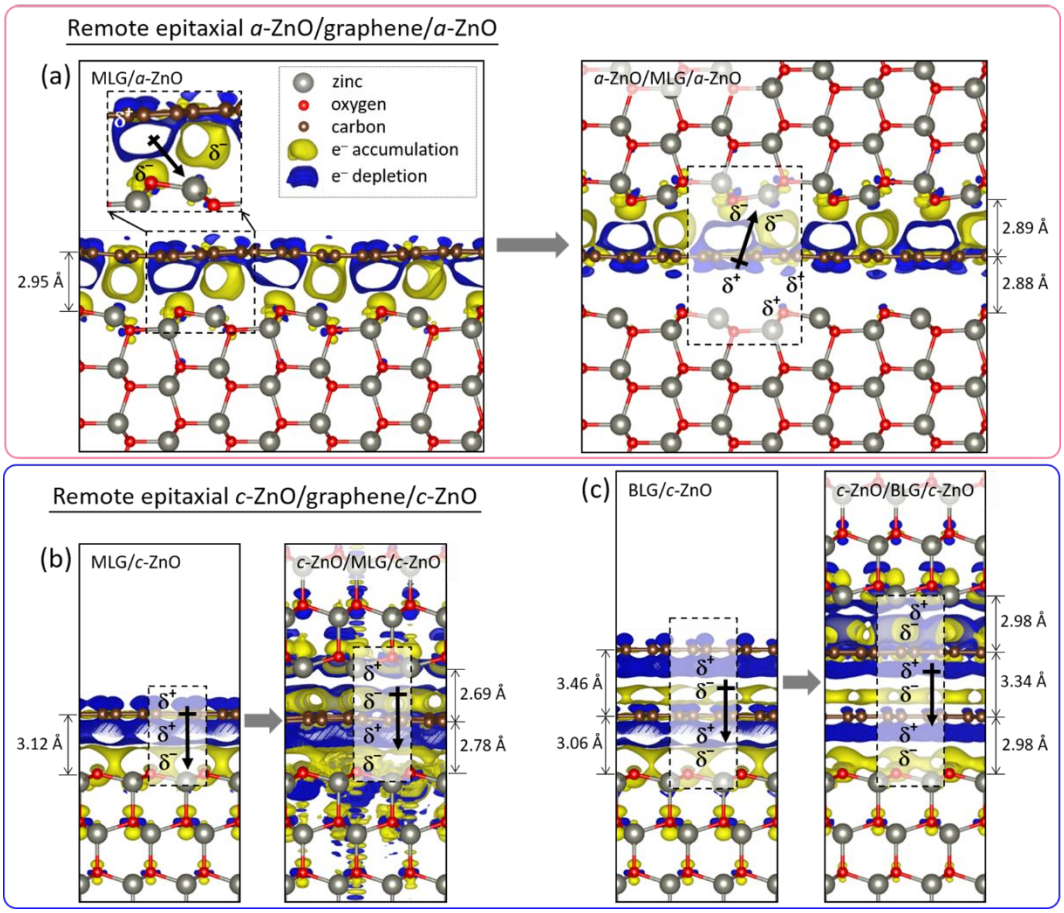

Fig. 4. Atomic structure and charge density difference (ΔCD) of remote homoepitaxial (a) *a*-ZnO/MLG/*a*-ZnO, (b) *c*-ZnO/MLG/*c*-ZnO, and (c) *c*-ZnO/BLG/*c*-ZnO heterointerfaces. All the left panels show stable atomic configuration and ΔCD of substrates before remote epitaxy, while the right panels correspond to those of remote epitaxial heterointerfaces after the overlayer growth. The ΔCDs were depicted at isosurface levels of ±0.0002 e/bohr^3. The yellow and blue isosurfaces stand for the electron accumulation and depletion regions, respectively. The dot-line boxes are chosen to represent repeating unit, where partial charges resulting from electron accumulation and depletion are denoted with δ^- and δ^+, respectively. The bond dipoles of '+→' marked in the dot-line boxes denotes the electric dipoles with Lewis notation to describe electric field direction and bond polarity.

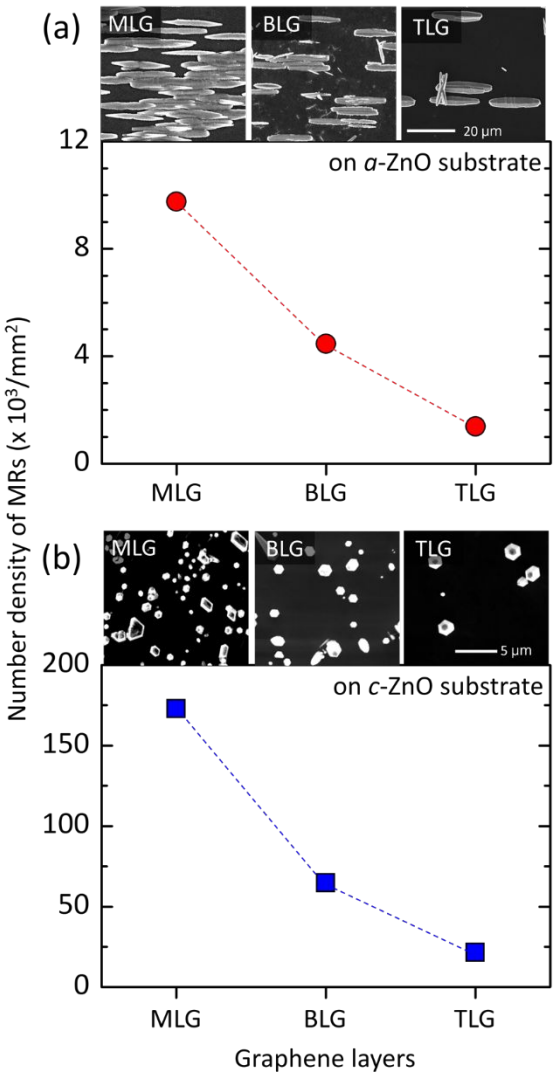

Fig. 5. Effect of remote epitaxial gap and substrate orientation on number density of remote homoepitaxial MRs. The number density of (a) horizontal and (b) vertical ZnO MRs, grown on *a*- and *c*-ZnO substrates, respectively, which was plotted as a function of graphene interlayer thickness that corresponds to remote epitaxial gap. Insets are a series of plan-view SEM images of MRs grown on different graphene thickness.

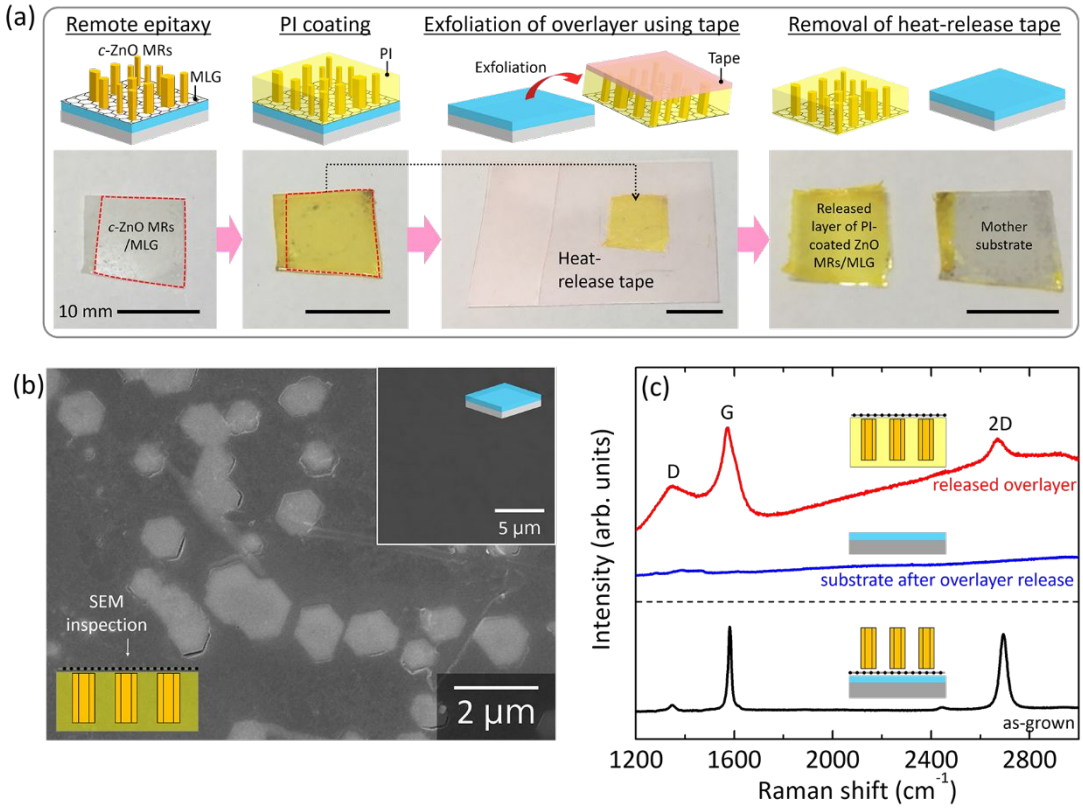

Fig. 6. Transferrable remote homoepitaxial ZnO MRs overlayer. (a) Schematic illustrations depicting exfoliation process of *c*-ZnO MRs overlayer via PI-supported peeling-off technique using heat-release tape (upper images) and the corresponding photographs displaying the substrate and the released overlayer after each process (lower images). (b) SEM image of the released backside surface of *c*-ZnO MRs supported with PI. Inset SEM image shows the surface of the *c*-ZnO substrate after the exfoliation process. (c) Raman spectra of the as-grown remote homoepitaxial c-ZnO MRs/graphene/*c*-ZnO substrate before exfoliation (bottom black line), substrate after overlayer release (middle blue line), and the released backside surface of the TLG/PI-filled *c*-ZnO MRs overlayer (top red line).

`

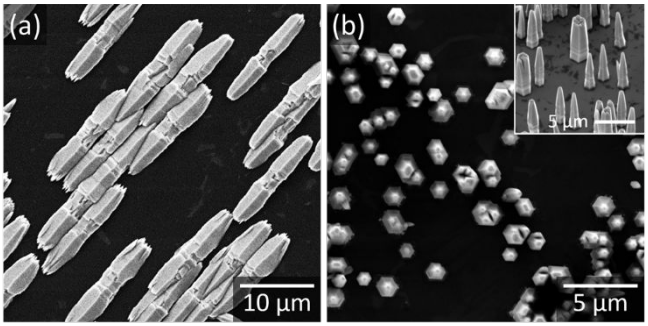

Fig. 7. Regeneration of substrate for remote homoepitaxy. Plan-view FE-SEM images of ZnO MR arrays grown on reused (a) *a*-ZnO and (b) *c*-ZnO substrates coated with MLG interlayer. Inset in (b) is tilt-view FE-SEM image.